



Universal Nanothin Silk Coatings via Controlled Spidroin Self-Assembly

Journal:	<i>Biomaterials Science</i>
Manuscript ID	BM-ART-09-2018-001186.R1
Article Type:	Paper
Date Submitted by the Author:	12-Dec-2018
Complete List of Authors:	Zha, Runye; Rensselaer Polytechnic Institute, Chemical & Biological Engineering Delparastan, Peyman; University of California, Berkeley, Materials Science and Engineering Fink, Tanner; Rensselaer Polytechnic Institute, Chemical & Biological Engineering Bauer, Joschka; University of Bayreuth, Biomaterialien Scheibel, Thomas; University Bayreuth, Biomaterialien Messersmith, Phillip; University of California, Berkeley, Bioengineering and Materials Science and Engineering



Universal Nanothin Silk Coatings via Controlled Spidroin Self-Assembly

R. Helen Zha,^{*a} Peyman Delparastan,^b Tanner D. Fink,^a Joschka Bauer,^c Thomas Scheibel,^c Phillip B. Messersmith^b

Received 00th December 2018,
Accepted 00th January 20xx

DOI: 10.1039/x0xx00000x

www.rsc.org/

Robust, biocompatible, and facile coatings are promising for improving the *in vivo* performance of medical implants and devices. Here, we demonstrate the formation of nanothin silk coatings by leveraging the biomimetic self-assembly of eADF(C16), an amphiphilic recombinant protein based on the *Araneus diadematus* dragline spidroin ADF4. These coatings result from concurrent adsorption and supramolecular assembly of eADF4(C16) induced by KH_2PO_4 , thereby providing a mild one-pot coating strategy in which coating rate can be controlled by protein and KH_2PO_4 concentration. The thickness of coatings range from 2 – 30 nm depending on time immersed in the aqueous coating solution. Coatings can be formed on hydrophobic and hydrophilic substrates regardless of surface chemistry and without requiring specialized surface activation. Moreover, coatings appear to be stable through vigorous rinsing and prolonged agitation in water. Grazing incidence wide angle X-ray scattering, single-molecule force spectroscopy, and Congo red staining techniques confirm the formation of β -sheet nanocrystals within the eADF4(C16) coating, which contributes to the cohesive and adhesive stability of the material. Coatings are exceptionally smooth in the dry state and are hydrophilic regardless of substrate hydrophobicity. In aqueous conditions, nanothin silk coatings exhibit the properties of a hydrogel material.

Introduction

The clinical success of biomedical materials and devices depends significantly on their surface properties. For example, hydrogel-coated catheters provide increased patient comfort¹ and can reduce bacterial encrustation when used in conjunction with antimicrobial agents.² Such surface modifications can potentially reduce the rate of catheter-associated urinary tract infections, which account for up to 40% of healthcare-associated infections in the U.S.³ For vascular stents, coatings that improve biocompatibility or elute therapeutics have demonstrated efficacy in reducing restenosis.⁴ Furthermore, biomedical coatings that inhibit fibrosis and inflammation are beneficial for maintaining the long-term performance and sensitivity of biosensors, such as implantable glucose monitors^{5,6} and neural electrodes.⁷

Current approaches towards surface modification include the use of covalent chemistries, such as silane coupling or “grafting from” polymerization. Other approaches include high energy UV or plasma treatment, layer-by-layer deposition, self-assembled monolayer formation, and dip or spin coating. These

strategies are typically multi-step processes that are substrate-dependent.⁸ Thus, individual optimization is required for chemically or topologically distinct surfaces. For example, covalent attachment can give adherent and conformal coatings on a variety of substrate geometries but is dependent on surface chemistry. Moreover, crosslinking agents used during covalent modification may be cytotoxic and persist in the material post-modification. Alternatively, dip or spin coating can be applied to a variety of substrate chemistries, but non-planar geometries or fine topological features can pose significant challenges. In contrast, “universal” coating strategies can modify materials independent of substrate chemical composition or physical characteristics.⁸ These coating strategies often leverage non-specific, non-covalent surface interactions. For example, mussel-inspired oxidative polymerization of dopamine in water has been studied extensively for generating versatile biomedical coatings.⁹⁻¹² Multiple mechanisms, including van der Waals interactions, hydrogen bonding, and metal-ion coordination underlie the adhesive and cohesive forces in polydopamine, resulting in dense and stable thin-film coatings that can be formed on virtually any surface.^{9,13,14}

In the past decade, silk has gained attention as a robust, biocompatible, and generally bioinert material.¹⁵⁻²⁰ Cell attachment to silkworm-derived silk protein (fibroin) and recombinant spider dragline silk protein (spidroin) is generally weak due to the lack of specific adhesion motifs.²¹⁻²⁴ For example, studies have indicated that fibroblasts adhere weakly to recombinant *Araneus diadematus* dragline spidroin surfaces, though roughness can improve cell adhesion.²² Furthermore,

^a Department of Chemical & Biological Engineering, Rensselaer Polytechnic Institute, 110 8th St., Troy, NY, 12180.

^b Department of Materials Science and Engineering, Department of Bioengineering, University of California – Berkeley, Berkeley, CA 94720.

^c Department for Biomaterials, University of Bayreuth, 95440 Bayreuth, Germany.

Electronic Supplementary Information (ESI) available: XPS spectra, long-term stability data, GIWAXS reductions, SEM images, AFM nanoindentation data, bacteria adhesion to drop-cast coatings. See DOI: 10.1039/x0xx00000x

silk generally exhibits low cytotoxicity and elicits lower inflammatory response than biomedical polymers such as collagen and polylactic acid.^{25–27} Silicone implants dip-coated in recombinant *A. diadematus* dragline spidroin exhibited reduced fibrous capsule formation and post-operative inflammation by inhibiting the proliferation of fibroblasts and CD68+ cells as well as lowering inflammatory cytokines expression.²⁸ With regards to biodegradability, though silk is a protein-based material, studies have shown that silk materials can persist *in vivo* depending on their morphology and the respective tissue environment from weeks to several months.²⁸

Given these biomedical properties, silk-based universal coatings could be a potent surface modification strategy for improving the performance of indwelling biomedical devices. Many properties of silk result from its protein primary structure, which contains a low-complexity repetitive core domain (Figure 1A).^{29–33} This core domain is amphiphilic, resembling a segmented copolymer with alternating hydrophobic blocks that form β -sheet nanocrystals and hydrophilic blocks that act as an amorphous matrix (Figure 1B). Consequently, silk materials are elastomers with β -sheet nanocrystals acting as supramolecular crosslinks.^{34,35} In the natural spinning process, silk proteins solubilized in an aqueous spinning dope undergo self-assembly to form these elastomers in response to kosmotropic factors, including an influx of phosphate anions.^{17,33,36–38} In the present work, we leverage this bioinspired self-assembly phenomenon of recombinant spidroins to generate nanothin spidroin coatings with adhesive and cohesive stability. We demonstrate that this coating process occurs on hydrophilic as well as hydrophobic substrates without requiring specialized surface preparation. We furthermore show that these coatings resist biofouling by *Escherichia coli* and *Staphylococcus epidermidis* bacteria, thus suggesting that controlled silk protein self-assembly can be a universal surface modification strategy for biomedical applications.

Results and Discussion

Coating Formation by Spidroin Self-Assembly

The formation of nanothin coatings via aqueous self-assembly of silk protein was explored using eADF4(C16), a recombinant spidroin that mimics the repetitive core domain of ADF4, a major ampulate dragline spidroin produced by *A. diadematus*.^{31,39,40} This 47.7 kDa protein was obtained from AMSilk GmbH and consists of 16 repeats of an amphiphilic 35-mer sequence with an artificial N-terminal T7 tag (Figure 1C). When solubilized, eADF4(C16) is an intrinsically disordered protein and is expected to more readily adopt conformations that favourably interact with a variety of surfaces. Additionally, eADF4(C16) can self-assemble into an insoluble supramolecular material upon exposure to kosmotropic factors.^{39,41,42} Each repeat contains a block of 8 alanine residues which can form β -sheets that further stack into inter- and intramolecular nanocrystals through hydrophobic interaction of the alanine side chains.^{43,44} These nanocrystals act as rigid crosslinks for the amorphous matrix formed by the hydrophilic portion of each

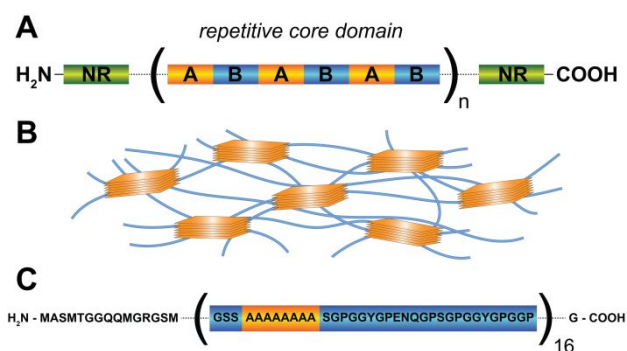
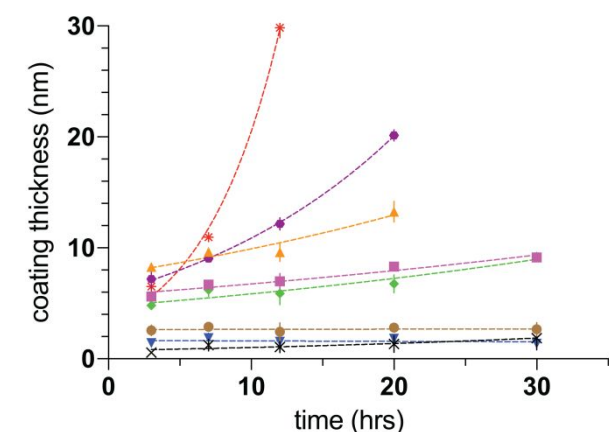


Figure 1. A) Illustration of native spidroin primary structure showing the repetitive core domain and non-repetitive (NR) terminal domains. B) Illustration of the elastomeric silk network, where hydrophobic β -sheet nanocrystals (orange) are embedded within a hydrophilic amorphous matrix (blue). C) Full sequence of eADF4(C16), a recombinant spidroin that mimics the repetitive core domain of ADF4 dragline spidroin of *A. diadematus*. This protein does not contain the NR domains of the native spidroin but does include an N-terminal T-7 tag as shown.

repeat, which contains a glutamic acid that increases protein solubility and is rich in glycine, proline, and serine. Moreover, the GPGXX motifs (where X is glycine, tyrosine, or serine) in the hydrophilic block can form β -turn spirals which contribute to the elasticity of the amorphous matrix.^{16,30} Due to its high propensity for aggregation, eADF4(C16) used in our studies was initially solubilized at 2.5 mg/mL in an aqueous 6 M solution of guanidinium thiocyanate (GITC), a chaotropic salt, for 60 mins under gentle inversion. The solution was then dialyzed into 25 mM bicine buffer at pH 8.5 with 100 mM NaCl as a stock solution. To prevent premature aggregation, these stock eADF4(C16) solutions were stored at 4 °C for no longer than 5 days before usage and were centrifuged at 8400 rcf for 30 mins to remove large protein aggregates immediately prior to use.

The *ex vivo* aqueous self-assembly of eADF4(C16) has been studied previously by Scheibel and coworkers.^{39,41,42,45–48} Their research demonstrated the formation of nanofibers due to 1-dimensional stacking of β -sheets in buffers containing < 300 mM phosphate ion concentration.^{39,41,45,46,49} The eADF4(C16) nanofibers were measured to be 2–3 nm thick by AFM imaging, approximately 10 nm wide by transmission electron microscopy (TEM), and several microns in length.⁴¹ eADF4(C16) nanofibers exhibit cross- β structure, where β -strands are orthogonally oriented to the fiber long axis. The self-assembly rate of eADF4(C16) increases at elevated temperature,³⁹ which facilitates secondary structure formation by entropically driving the dehydration of water molecules from the protein backbone. Methanol has similarly been used to initiate nanofiber formation, and hydrogellation of eADF4(C16) solutions within one week has been observed at 5 – 30 mg/mL spidroin concentration in the presence of methanol.⁵⁰

In our studies, phosphate-initiated self-assembly of aqueous eADF4(C16) was used to coat substrates with nanothin spidroin films in a simple and mild process. eADF4(C16) solutions were diluted from stock and used at 0.5 – 2 mg/mL with up to 200



Symbol	eADF4(C16) (mg/mL)	NaCl (mM)	KH ₂ PO ₄ (mM)	Temp (°C)	
*	1	100	200	25	Coating hazy after 12 hrs
•	0.5	100	200	25	Coating hazy after 20 hrs
▲	2	100	100	25	Coating hazy after 20 hrs
■	1	100	100	25	
◆	0.5	100	100	25	
●	1	0	0	37	
▼	1	100	0	25	
×	1	0	0	25	

Figure 2. Plot of dry coating thickness after 3, 7, 12, 20, and 30 hrs immersion time in coating solution as measured by ellipsometry. Coating conditions are listed in the table shown. Dotted lines represent exponential fits to data points. For coating conditions with high eADF4(C16) or KH₂PO₄ concentrations, coatings became visibly hazy at longer time points and thickness could not be accurately determined by ellipsometry.

mM KH₂PO₄ added to induce β -sheet formation. We observed that planar TiO₂ substrates immersed in these solutions became coated by a layer of eADF4(C16) which remained even after vigorous rinsing with water. X-ray photoelectron spectroscopy (XPS) of TiO₂ samples coated by immersion in 2 mg/mL eADF4(C16) with 100 mM KH₂PO₄ for 30 hrs showed a nitrogen-to-carbon signal ratio (N/C) of 0.30, which corresponds to the calculated N/C = 0.305 of eADF4(C16) based on sequence. Deconvolution of the carbon signal in high resolution XPS (283 – 291 eV binding energy) revealed a strong amide signal at 288.2 eV as well as signals from aliphatic, aromatic, and α -carbons (Figure S1). In this case, no Ti signals were seen from the underlying substrate, suggesting that the coating thickness was likely greater than the approximately 10 nm XPS probe depth.

Solution Conditions and Coating Growth

Spectroscopic ellipsometry was used to measure coating thickness with varying coating conditions, such as substrate immersion time, spidroin concentration, temperature, and salt content. When TiO₂ substrates were immersed in eADF4(C16) solution without KH₂PO₄ at room temperature, a spidroin layer < 2 nm thick was measured on surfaces after the coating process. The thickness of this layer did not increase with coating time (Figure 2). Raising the temperature to 37 °C during coating

resulted in slightly increased thickness (~ 3 nm) but did not produce noticeable coating growth over time. However, adding KH₂PO₄ into the coating solution resulted in spidroin coatings that grew in thickness over time. For example, with a solution containing 0.5 mg/mL eADF4(C16), 100 mM NaCl, and 100 mM KH₂PO₄, coating thickness increased from 4.8 ± 0.4 nm after 3 hrs to 9.2 ± 0.4 nm after 30 hrs. While minimal change in coating growth rate was observed when the eADF4(C16) concentration was increased to 1 mg/mL, further doubling the concentration to 2 mg/mL yielded a noticeable increase in coating rate. The concentration of KH₂PO₄ was observed to have the largest effect on coating thickness, with coatings formed in 1 mg/mL eADF4(C16) with 100 mM NaCl and 200 mM KH₂PO₄ growing up to 29.8 ± 0.9 nm after 12 hrs.

Our finding differs from previous work by Kaplan and coworkers on stepwise deposition of *Bombyx mori* silk fibroin coatings.^{51,52} In these works, substrates were dipped in a dilute silk fibroin solution for several minutes, then washed with a water/methanol mixture and dried with nitrogen gas. This process was repeated to build a layer-by-layer coating. It was observed that though coating thickness increased linearly with each additional layer, protein deposition for each layer reached a plateau within minutes and the drying step was required for continued protein addition in the subsequent layer.⁵¹ These results are consistent with a typical protein adsorption model,⁵³⁻⁵⁵ which shows a plateau as the surface reaches saturation, as observed with proteins such as α -amylase.⁵⁶ In our coating process, adsorption occurs simultaneously with self-assembly in solution as well as at the solid-liquid interface. Previous studies have shown that the aqueous self-assembly of eADF4(C16) into nanofibers follows a Finke-Watzky two-step model.^{39,57} The first step is the slow assembly of protein monomers to form a “catalytic” nucleus, and the second step is rapid elongation by addition of protein monomers to an actively growing end. This two-step self-assembly can be fitted to a logistic function with an initially exponential growth, and higher phosphate ion concentration has been shown to decrease the time constant.³⁹ While our findings of coating growth are qualitatively consistent with this model, the interplay between solution-phase self-assembly, adsorption of spidroin monomers or aggregates to the surface, and surface-bound assembly (Figure S2) requires further study to understand the mechanisms driving coating formation.

In our studies, coatings typically appeared colorless and transparent. However, with increased eADF4(C16) concentration (2 mg/mL) or KH₂PO₄ concentration (200 mM), coatings became visibly hazy at long coating times and white precipitates were observed in solution. The scattering of these coatings prevented accurate thickness measurement by ellipsometry. We determined that a slightly lower eADF4(C16) concentration (0.5 mg/mL) combined with a high KH₂PO₄ concentration (200 mM) and 100 mM NaCl in pH 8.5 bicine buffer provided optimal conditions for high quality coatings at low material usage and acceptable growth rates. These solution parameters were used for all subsequent studies unless otherwise stated.

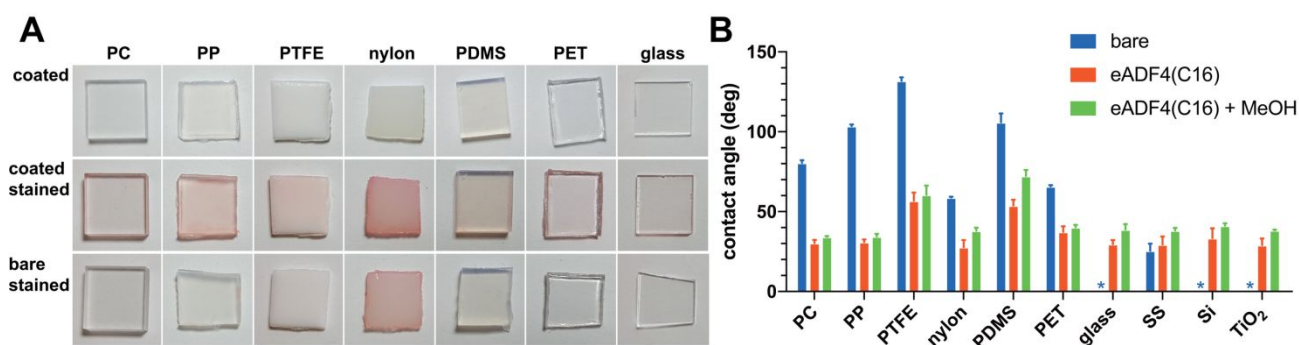


Figure 3. A) Images showing the appearance of eADF4(C16)-coated substrates with and without Congo red staining. Bare substrates stained with Congo red are shown in the bottom row as controls. B) Water contact angles on substrates before coating with eADF4(C16) and after eADF4(C16) coating with and without methanol post-treatment. Completely wetting samples (contact angle $< 20^\circ$) are indicated by *. Bare substrates were cleaned as described in the Experimental section, and at least 3 samples were measured for each substrate type.

Coating Stability

The apparent ability of our nanothin spidroin coatings to withstand vigorous rinsing before being dried suggests that the coating exhibits adhesive and cohesive stability. We further investigated the aqueous stability of spidroin coatings by agitating eADF4(C16)-coated TiO₂ samples in HEPES buffer (pH 7.4, 150 mM NaCl, 37 °C) at 60 RPM in an orbital shaker. After 1, 2, 4, 6, 8, and 11 days of agitation, samples were gently rinsed with water and dried using nitrogen gas prior to characterizing the change in coating thickness with ellipsometry. We observed that coating thickness decreased by an average of 14% after 1 d (Figure S3). However, coating thickness remained relatively constant afterwards for the duration of the 11-day study. These results suggest that the coating does not dissolve or detach from the surface over time. The initial decrease in coating thickness may result from further conformation change or molecular rearrangement during aqueous annealing, which is known to occur in natural spider webs during a phenomenon called “supercontraction”.⁵⁸

The stability of the eADF4(C16) coatings is surprising considering the noncovalent nature of interactions with the surface, which may include van der Waals forces and hydrophobic interactions for hydrophobic substrates, hydrogen bonding for oxide or polar substrates, and electrostatic attraction for charged substrates. The role of multiple noncovalent interactions as a driving force for generating substrate-independent polymer coatings is known. However, such polymer coatings typically require chemical crosslinking to enhance stability, as noncovalent forces are usually too weak to for effective surface anchoring in practical applications.⁸ It is likely that a multiplicity of surface-spidroin interactions in conjunction with the cohesive strength of the elastomeric silk network enables one-pot formation of a stable coating as demonstrated in our studies. Using phosphate ions to induce β -sheet crystallization can be a supramolecular stabilization strategy analogous to the chemical crosslinking of polymer coatings. In our work, evolution of coating adhesion and cohesion occurs simultaneously. Moreover, the relatively gradual manner of our coating process compared to methods

such as spin-coating or dip-coating may allow spidroins to adopt maximally favorable interactions with the surface and thus further enhance coating stability. This hypothesis is supported by the well-known phenomenon of protein spreading, in which proteins adsorbed at a solid-liquid interface increase in footprint on the timescale of minutes to hours.^{59,60}

Substrate Dependence

Interestingly, proteins that are predominantly unordered have been known to play a role in the substrate-independent adhesion of mussels under water.^{61,62} The mussel foot proteins mfp-1, mfp-2, and mfp-3 exhibit significant extended random coil structure,⁶¹ though some amount of local order cannot be excluded. This conformation is thought to allow the proteins to readily conform to best interact with a variety of substrates to mediate surface fouling by the byssal holdfast. Furthermore, studies have shown that mussel adhesive proteins can undergo structural rearrangement during adsorption, whereby β -sheet content increases in conjunction with loss of random coil structure.⁶² Since aqueous eADF4(C16) is also a predominantly disordered protein that can undergo β -sheet formation, it is possible that similar mechanisms can facilitate the adhesion of eADF4(C16) to a variety of surfaces.

We examined the formation of eADF4(C16) coatings via phosphate-initiated self-assembly on a series of hydrophobic, hydrophilic, organic, and inorganic substrates. Glass, stainless steel, silicon, and TiO₂ substrates were cleaned by sonicating for 15 mins each in a sequence of solvents (10% Simple Green degreaser, ultrapure water, isopropanol, acetone, ultrapure water), dried with nitrogen gas, and further cleaned by UV-ozone treatment prior to coating. Nylon, polydimethylsiloxane (PDMS), polycarbonate (PC), poly(ethylene terephthalate) (PET), polypropylene (PP), and polytetrafluoroethylene (PTFE) were similarly cleaned by sonication (without acetone) but were not cleaned by UV-ozone. To visualize eADF4(C16) coatings on clear or white substrates, Congo red was used to stain for β -sheet structures. After 30 hrs immersion in the coating solution, we found that substrates were covered by eADF4(C16) regardless of surface chemistry. Coatings appeared

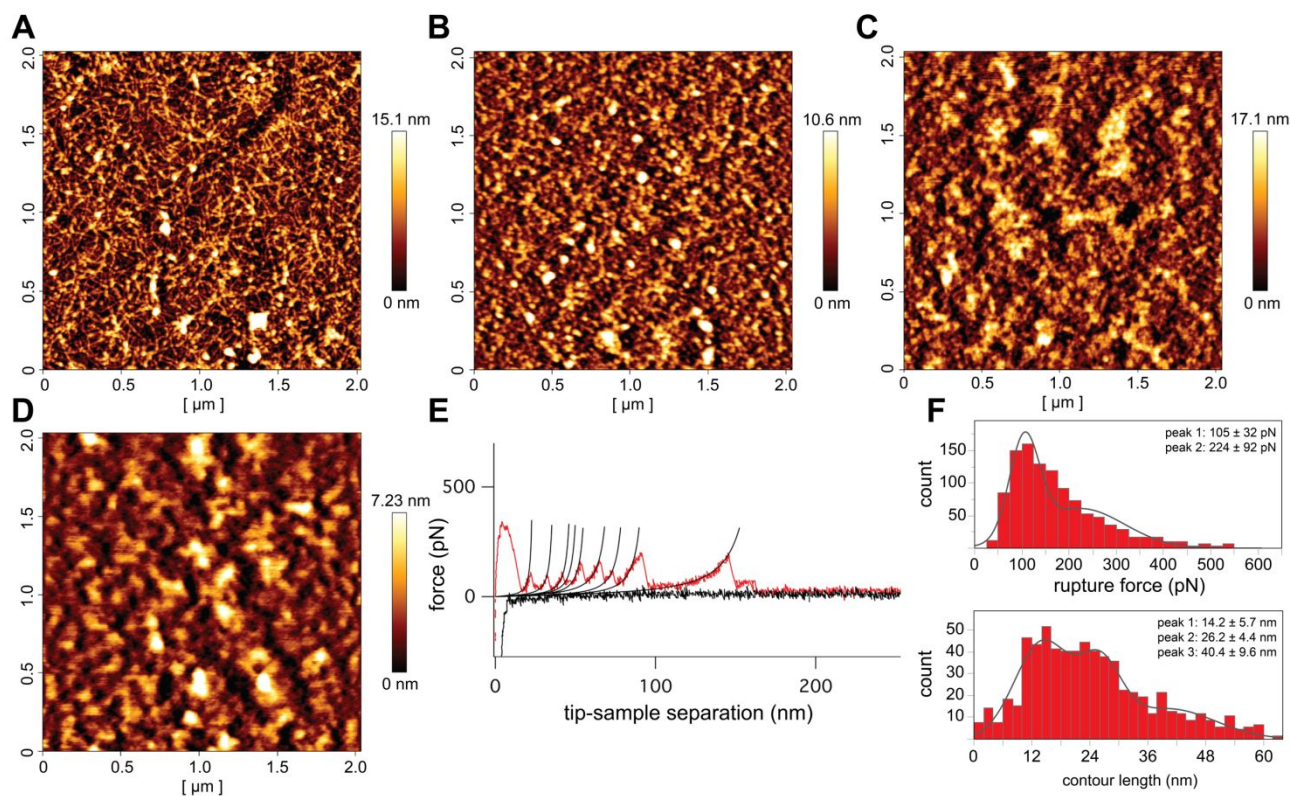


Figure 4. AFM height images of the surface morphology of dry eADF4(C16) coatings after A) 3 hrs, B) 7 hrs, and C) 20 hrs immersion in coating solution. D) Height image of a 3 hrs coating when imaged in aqueous 150 mM NaCl solution. E) A representative force-extension trace (retraction in red) obtained in single-molecule AFM force spectroscopy on eADF4(C16) coatings showing a typical sawtooth pattern (red curve) indicative of sequential rupture or unfolding events. A WLC model was fit to these events (black curves) and F) distributions of rupture forces and contour lengths obtained from WLC fits are shown. Peak rupture forces and contour lengths were determined through curve fitting analysis of histograms.

clear and colorless, with Congo red staining revealing a red tint to coated samples (Figure 3A).

We compared the wettability of coated and uncoated substrates by measuring the static contact angle of water. eADF4(C16)-coated substrates were hydrophilic with a contact angle of $\sim 30^\circ$ regardless of initial substrate wettability (Figure 3B). eADF4(C16)-coated substrates were additionally immersed in methanol for 1 hr to further induce β -sheet formation. Coating hydrophobicity increased only slightly after methanol treatment. PTFE and PDMS were exceptions and showed contact angles of $50\text{--}60^\circ$ after coating, which was still a large increase in hydrophilicity compared to the bare substrates. However, eADF4(C16) coatings on PDMS made hydrophilic by UV-ozone treatment prior to coating exhibited a contact angle of $38^\circ \pm 3^\circ$, which is more in line with results found for coatings on other substrates (Figure 3B). This suggests the potential role of surface energy on coating properties in certain scenarios. It should be noted that PTFE and PDMS have the lowest surface energies (~ 20 mN/m) compared to other substrates tested (> 30 mN/m). Thus, while nanothin spidroin coatings seem to be insensitive to substrates with a threshold surface energy, substrates with extremely low surface energy may give rise to coatings with different morphologies and properties. It is known that in eADF4(C16) films, the hydrophilic and hydrophobic amino acid blocks undergo phase separation and

that surface hydrophobicity may influence the distribution of domains, giving rise to materials with different wettability.⁶³ Furthermore, surfaces with extremely low surface energy may potentially induce different secondary structures during the coating assembly process. Thus, the effect of surface energy on the coating process should be comprehensively studied in future works.

Morphology and Molecular Structure

Scanning electron microscopy (SEM) was used to image the morphology of eADF4(C16)-coated TiO_2 . Coatings appeared smooth and exceptionally featureless (Figure S4). No particles could be seen on the surface despite the visible aggregation of spidroins in solution with high eADF4(C16) or phosphate concentration, suggesting that large aggregates did not adhere to the coating. However, SEM did not provide sufficient resolution and contrast to probe the nanoscale surface morphology of eADF4(C16) coatings. Thus, atomic force microscopy (AFM) was used to image the topology of dry coatings after various coating times (Figures 4A – 4C). After 3 hrs of immersion in the coating solution, TiO_2 surfaces appeared to be covered by nanofibers approximately 12 nm wide, which is consistent with the dimensions of solution-phase eADF4(C16) nanofibers studied by Scheibel and coworkers.⁴¹ At longer

ARTICLE

Biomaterials Science

coating times, the nanofiber morphology became less distinguishable and could not be observed after coating growth for 20 hrs. The root mean square roughness of coatings ranged from 3-5 nm. Interestingly, AFM imaging in saline showed that the features of the eADF4(C16) coating swell significantly. For example, 3 hr coatings exhibiting nanofiber morphology in the dry state did not show distinguishable nanofibers when hydrated, and the surface appeared as a soft, amorphous material (Figure 4D).

Grazing incidence wide angle X-ray scattering (GIWAXS) was performed at the 12-ID Soft Matter Interfaces beamline at National Synchrotron Light Source II (NSLS-II) to characterize the molecular-scale organization of eADF4(C16) coatings. eADF4(C16) coated onto silicon wafers with an approximately 2 nm native oxide layer for 24 hrs were exposed to a beam energy of 16.1 keV ($\lambda = 0.77 \text{ \AA}$) at an incidence angle of 0.1° . 2D scattering patterns were collected (Figure S5) and were converted into (q_r, q_z) space (Figure 5), where q_r is the in-plane scattering from the sample and q_z is the out-of-plane scattering from the sample. The (q_r, q_z) scattering images were furthermore radially reduced to a 1D dataset of intensity vs. $|q|$ (Figure S5). We observed a set of overlapping reflections in the range of $0.8 \text{ \AA}^{-1} < |q| < 1.8 \text{ \AA}^{-1}$ arising from the eADF4(C16) coating. After deconvolution, scattering peaks at 1.15 \AA^{-1} and 1.43 \AA^{-1} could be distinguished (Figure S5). These peaks are consistent, respectively, with the (200) and (120) Bragg reflections of β (L-polyalanine) crystals and have been previously observed in silk fibers as well as in drop-cast eADF4(C16) samples after methanol treatment.^{44,64-67} Additionally, a weak Bragg peak can be seen at 1.68 \AA^{-1} , potentially corresponding to the (121) reflection of β -sheet crystals in various silk fibroins.^{44,66} While the symmetry of β -sheet crystals in native silk has been debated,^{67,68} assuming an orthorhombic crystal structure as previously observed in multiple silk fibroins^{44,66,67} allows the lattice parameters $a = 10.93 \text{ \AA}$, $b = 9.60 \text{ \AA}$, and $c = 7.12 \text{ \AA}$ to be calculated (see equations described in the Experimental section). Each unit cell is thought to contain two pairs of hydrogen-bonded peptide chains,⁶⁶ with the a and b axes roughly corresponding to the β -sheet stacking direction (i.e. the direction of the side chains) and the hydrogen bonding direction, respectively.⁴⁴ Thus, the inter-sheet distance is aptly approximated by $a/2 = 5.46 \text{ \AA}$ and the inter-strand distance can be approximated by $b/2 = 4.80 \text{ \AA}$. Furthermore, a broad amorphous halo ($|q| = 1.36 \text{ \AA}^{-1}$) could be fitted in the deconvolution of the 1D scattering data. These results agree well with previous X-ray diffraction (XRD) studies of native silk fibroin^{44,66,67} as well as grazing incidence XRD studies of thick methanol-treated drop-cast eADF4(C16) coatings.⁶⁴

By comparing the peak areas of the crystalline reflections to the total peak area, we can estimate the percent crystallinity (X_c) in the eADF4(C16) coatings with the equation:

$$X_c = \frac{A_{200} + A_{120} + A_{121}}{A_{200} + A_{120} + A_{121} + A_{amorph}}$$

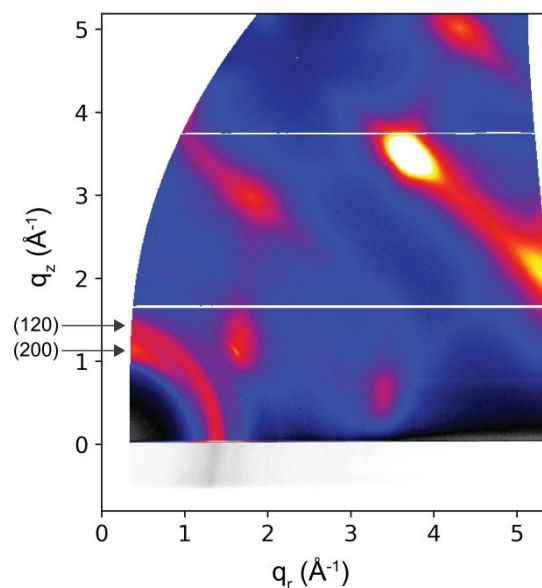


Figure 5. 2D scattering image obtained from GIWAXS of dry eADF4(C16) coatings on silicon wafer (24 hrs coating time) after conversion to (q_r, q_z) space, showing anisotropic scattering by the (200) planes of β -sheet crystallites along the q_z axis. Scattering arising from the eADF4(C16) coating occurs in the range of $0.8 \text{ \AA}^{-1} < |q| < 1.8 \text{ \AA}^{-1}$, while scattering from the underlying silicon and native oxide layer is visible at $|q| > 1.8 \text{ \AA}^{-1}$.

For silicon substrates coated for 24 hrs with 0.5 mg/mL eADF4(C16) and 200 mM KH_2PO_4 , $X_c = 36\%$. It should be noted that this X_c calculation is subject to some error due to the overlap of the amorphous halo with crystalline reflections. Nevertheless, our X_c values compare reasonably with the β -sheet content found in methanol-treated eADF4(C16) sheets by Fourier-transform infrared spectroscopy.⁶⁹ Interestingly, X_c does not change significantly for coatings grown for shorter time periods (Figure S5), suggesting that the silk material added over time has similar structural composition. Furthermore, we observed from the 2D GIWAXS image that the scattering of the (200) and (121) reflections appear to be anisotropic (Figures 5A and S5), with the $|q| = 1.15 \text{ \AA}^{-1}$ arc for the (200) reflection more strongly visible near the q_z axis than the q_r axis. In line with XRD studies of various silk fibers,^{44,66,67} the (121) reflection is more strongly visible at an angle to the (200) reflection between the q_z and q_r axes. This anisotropy suggests that the β -sheets preferentially lied parallel to the surface. Such an orientation would present a large crystallite area to interact with the surface and may contribute to the adhesive stability of the coating. In comparison, the broad amorphous halo observed at $|q| = 1.36 \text{ \AA}^{-1}$, which partially overlaps with the (120) reflection, appears relatively constant in intensity along the q -arc and does not exhibit preferential orientation. Furthermore, GIWAXS studies of nanothin spidroin coatings assembled on TiO_2 showed similar results (Figure S6), suggesting that the observed β -crystal structure and orientation is not unique to the Si/SiO₂ substrate.

Micromechanical Properties by AFM

Silk is known for exceptional mechanical properties resulting from the elasticity of the amorphous matrix in conjunction with the stiffness and supramolecular crosslinking provided by the β -sheet nanocrystals.^{34,35,70} AFM nanoindentation was used to measure the stiffness of hydrated nanothin eADF4(C16) coatings on TiO₂. A soft silicon cantilever with a spring constant of 0.2 N/m and a spherical probe tip 23 nm in diameter was used to indent eADF4(C16) coatings at a velocity of 1000 nm/s (Figure S7). Assuming negligible interactions between the indenter and coating, we fitted loading and unloading force-distance curves to a Hertz model⁷¹ with a Poisson's ratio of 0.5 (for incompressible rubber-like materials) to extract the Young's modulus (Figure S7). For coatings approximately 20 nm thick, a

Young's modulus of 2.9 ± 1.4 MPa was found in water. In comparison, native *A. diadematus* dragline silk threads are expected to have stiffness values close to 10 GPa. However, silk fibers are known to exhibit significantly lower stiffness when hydrated,⁷² as the amorphous domains in silk are hydrophilic. Furthermore, it is known that silk films generally demonstrate decreased strength and stiffness compared to native silk fibers, as the mechanical properties of silk threads are heavily influenced by the spinning process.¹⁷ For example, tensile measurements of drop-cast eADF4(C16) films have shown Young's modulus values of 2-4 GPa,⁷³ and AFM nanoindentation of dried eADF4(C16) nanoparticles fabricated by salting out has demonstrated a modulus of 0.8 GPa.⁷⁴ Our results for hydrated nanothin eADF4(C16) coatings formed by self-assembly are

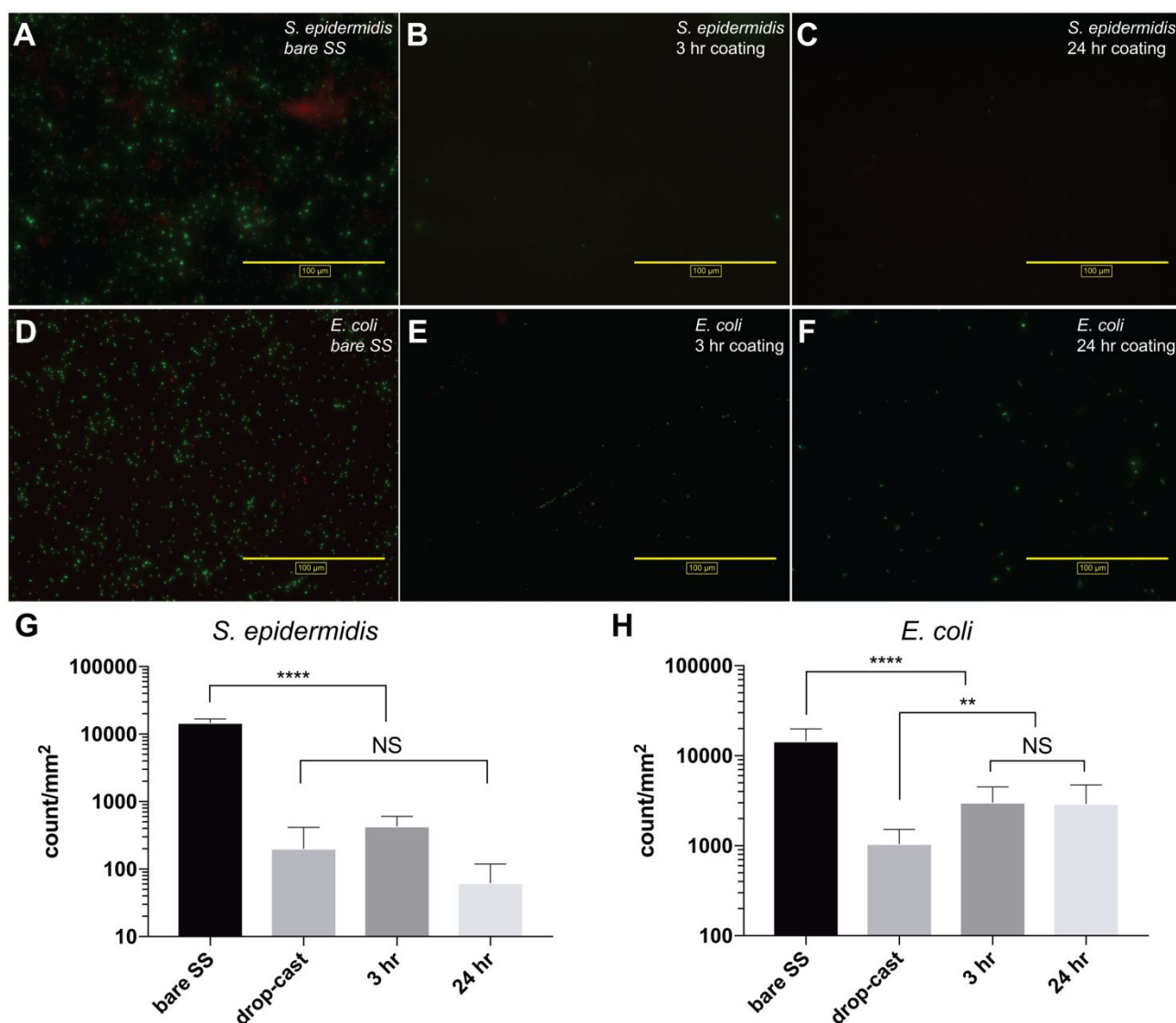


Figure 6. Fluorescence microscopy images of (A-C) *S. epidermidis* and (D-F) *E. coli* adhered to eADF4(C16)-coated and bare stainless steel. Live (green) and dead (red) cells were stained using SYTO9 and propidium iodide. The number density of live (G) *S. epidermidis* and (H) *E. coli* cells on bare stainless steel, drop-cast coatings with methanol post-treatment, and nanothin eADF4(C16) coatings after 3 hrs or 24 hrs coating time was quantified by manual counting in ImageJ software. At least 10 images from each sample were counted (corresponding to 0.57 mm²), and 3 samples were examined per condition ($n = 3$). Statistical significance was determined using one-way ANOVA with a Tukey's multiple comparisons post hoc test, where $p < 0.0001$ (****), $p < 0.01$ (**), and $p > 0.05$ (NS – not significant).

comparable to previously published AFM nanoindentation measurements of eADF4(C16) nanoparticles in water, which exhibited a Young's modulus of approximately 3 MPa.⁷⁴ Furthermore, these findings are consistent with our hydrated AFM images suggesting that our eADF4(C16) coatings exist in aqueous environments as soft, hydrogel-like materials bound to the substrate surface.

AFM force spectroscopy was used to probe the mechanical properties of single molecules in nanothin eADF4(C16) coatings. Experiments were performed in ultrapure water using soft silicon nitride cantilevers after allowing the cantilever to equilibrate in solution for at least 30 minutes. The tip was brought in contact with the coating surface for a 1 s dwell time and was then retracted at a velocity of 1000 nm/s. The force exerted on the cantilever as the tip pulled away from the coating was recorded. As each measurement cycle required only 2 s, a JPK ForceBot 300 was used to record at least 50,000 force-distance curves per sample. No force was observed in >98% of pulling measurements, indicating that no molecules had attached to the probe. In a small percentage of experiments, sawtooth patterns were observed in the force-extension traces (Figure 4E). These sawtooth patterns are typical for crosslinked polymeric networks as well as proteins with modular structures and have been previously observed for spider and silkworm silk proteins.⁷⁵⁻⁷⁷ Here, each peak in the pattern represents a rupture or unfolding event that is preceded by force-induced protein chain extension. Each sequential rupture reveals previously unloaded chain segments, followed by further chain extension and unfolding of additional β -strands.

The rupture events were fitted using a worm-like chain model (WLC), which relates protein extension to the entropic force generated by that extension. Using WLC, contour length (L_c) and persistence length (p) parameters were extracted for each rupture. For force spectroscopy of polypeptides, a persistence length near 0.4 nm is expected for single chains at high force.^{76,78} Thus, for quantitative analysis, we considered only data which gave $p = 0.4$ nm in the WLC fit, which corresponds to peaks in which rupture arises from single molecule interactions. The distributions of L_c and rupture force from this dataset were plotted as a histogram and fitted to identify peaks (Figure 4F). Our analysis indicates that the primary rupture force observed was 105 ± 32 pN and a secondary peak in rupture force occurred at 224 ± 92 pN. The peak contour lengths observed were 14.2 ± 5.7 nm, 26.2 ± 4.4 nm, and 40.4 ± 9.6 nm. Assuming these contour lengths are integer multiples of a common repeat unit, we obtain an average repeat unit length of 13.6 nm. This value is consistent with the calculated contour length of one 35-mer repeat unit in eADF4(C16) (13.3 nm) with a theoretical length of 0.38 nm per amino acid.^{76,79} Therefore, our results suggest that rupture events seen in single-molecule force spectroscopy correspond to the peeling of one or more β -strands from a β -sheet crystal, confirming that these β -sheet crystals play a critical role in the cohesion of polypeptides in the coating.

Analysis of Cell Adhesion

Studies have shown that mammalian cell adhesion to silk-based materials is generally poor. For example, BALB/3T3 mouse fibroblasts adhere poorly to eADF4(C16) hydrogels and films, though adhesion could be improved by increasing surface roughness or by adding RGD integrin binding motifs.^{22,80,81} Here, we investigated the adhesion of *Staphylococcus epidermidis* (gram-positive) and *Escherichia coli* (gram-negative) to eADF4(C16)-coated substrates. For our studies, stainless steel coupons were coated for either 3 hrs or 24 hrs with eADF4(C16) and were then incubated in 150 mM NaCl containing 1×10^8 cfu of each bacteria strain. Samples were incubated at 37 °C without agitation for 24 hrs in *S. epidermidis* and for 48 hrs in *E. coli*. The samples were then gently washed and stained with a propidium iodide/SYTO9 assay kit (ThermoFisher LIVE/DEAD BaLight Bacterial Viability Kit) for quantification of live and dead cells by fluorescence microscopy.

Our results indicate that bare stainless steel control samples incubated in *E. coli* and *S. epidermidis* showed significant amounts of bacterial fouling (Figure 6). Additionally, background staining was visible on samples exposed to *S. epidermidis* and cells appeared clustered, suggesting the initial stages of biofilm formation on these control samples. However, the presence of both *E. coli* and *S. epidermidis* was noticeably reduced on eADF4(C16)-coated surfaces. Manual quantification showed that the live *E. coli* and *S. epidermidis* counts were reduced by 79-92% and 97-99% on coated surfaces, respectively (Figure 6). Dead bacteria were not observed on coated surfaces, suggesting that the mechanism of resistance was not bactericidal. Interestingly, bacterial adhesion to samples coated for 3 hrs or 24 hrs did not differ significantly, though drop-cast eADF4(C16) coatings several hundred nanometers thick were slightly more effective in resisting *E. coli* adhesion than nanothin coating (Figure S8). Given the importance of biofouling resistance in numerous fields, the specific mechanisms of antifouling behavior in spider silk coatings merits further study in future works.

Conclusions

Our studies have demonstrated the formation of stable nanothin silk coatings via self-assembly of the recombinant spidroin eADF4(C16). These coatings result from one-pot adsorption and phosphate-induced supramolecular assembly of eADF4(C16) into a surface-bound hydrogel material. Surprisingly, coatings could be formed regardless of substrate chemistry, and pre-coating surface activation was not required. This universal adhesion results from non-specific, non-covalent interactions between the silk layer and the surface. Though eADF4(C16) cannot be considered "sticky" in a conventional sense, the formation of β -sheet crystallites within the silk material as supramolecular crosslinks in a robust elastomeric network likely enhances coating stability by distributing forces among multiple non-specific adhesion sites which may be individually weak.

Since the formation of eADF4(C16) coatings by controlled self-assembly occurs in mild, aqueous conditions without the use of chemical crosslinkers, our coating method can be a potential strategy towards biomedical surface functionalizing. As a proof-of-concept, the resistance of eADF4(C16) coatings to bacterial fouling was investigated using *S. epidermidis* and *E. coli*. Results suggest that these coatings resist bacterial adhesion and can therefore be promising for improving the performance of indwelling implants and devices.⁸²

The work presented here describes the basic process of coating formation as well as chemical, mechanical, and structural characterization of coating properties. Much remains to be explored regarding the mechanisms of coating assembly as a function of substrate properties, solution conditions, and protein sequence. For example, though the coating process appears to be tolerant of a wide range of substrates, surface energy undoubtedly has an effect on the adsorption kinetics of spidroins. Furthermore, an optimal rate of solution-phase spidroin aggregation, as determined by pH, salt content, and temperature, likely exists for coating formation. This hypothesis is suggested by the observation that coating growth is not observed without solution conditions that promote spidroin assembly. Lastly, generalizability of the coating phenomenon to other silk fibroins or β -sheet-forming proteins should be explored in context of the structure-forming motifs in the protein sequence. Future work to understand these factors in mechanism of coating formation, while outside the scope of the current work presented here, will be key to enabling the rational design of universal nanothin protein-based coatings.

Experimental

General Coating Procedure

Self-assembly of nanothin eADF4(C16) coatings was performed using the following generic procedure:

eADF4(C16) obtained from AMSilk GmbH as lyophilized powder was solubilized at 2.5 mg/mL in an aqueous 6 M guanidinium thiocyanate solution for 60 mins under gentle inversion. The solution was then dialyzed into 25 mM bicine buffer at pH 8.5 containing 100 mM NaCl. These stock solutions were stored at 4 °C for no longer than 5 days before usage, and solutions were centrifuged at 8400 rcf at 4 °C for 30 mins to remove protein aggregates immediately prior to use. eADF4(C16) concentration was then measured using a NanoDrop 2000 Spectrophotometer (Thermo Fisher, Waltham, MA) and diluted to the final coating concentration using 25 mM bicine buffer (pH 8.5) with 100 mM NaCl and various concentrations of KH_2PO_4 .

Polished silicon wafers (P/B, <100>) with approximately 2 nm native oxide layer and silicon wafers coated with 100 nm TiO_2 by e-beam evaporation were obtained from University Wafers (Boston, MA). Additionally, glass slides were obtained from Fisher Scientific (Hanover Park, IL), and mirror-polished stainless steel, nylon 6, PDMS, PC, PP, PET, and PTFE sheets were obtained from McMaster-Carr (Robbinsville, NJ). Prior to coating, TiO_2 , glass, stainless steel, and silicon coupons were

cleaned by sonicating for 15 mins each in 10% Simple Green Original degreaser (Sunshine Makers Inc., Huntington Beach, CA), ultrapure water, isopropanol, acetone, and ultrapure water. Substrates were then dried using a stream of nitrogen gas and were cleaned by UV-ozone treatment in a PSD Pro Series Benchtop Cleaner (Novascan Technologies, Boone, IA) for 5 mins immediately prior to immersion in the coating solution. Polymer substrates were similarly cleaned by sonication but were not exposed to acetone and UV-ozone.

Cleaned substrates were immersed in freshly prepared coating solution in small petri dishes, which were sealed by parafilm and placed on an incubated orbital shaker at 60 rpm. For coatings performed at elevated temperatures, a beaker of water was placed inside the shaker to further minimize evaporation over time. After completion of various coating times, substrates were removed from the coating solution, washed vigorously with ultrapure water from a squeeze bottle for at least 30 s, and dried using nitrogen gas stream. Care was taken to ensure that no drying occurred before the wash step.

Congo Red Staining

Nylon, PDMS, PTFE, PP, PET, PC, and glass coupons were cleaned and coated for 24 hrs in 0.5 mg/mL eADF4(C16) with 200 mM KH_2PO_4 in 25 mM bicine buffer (pH 8.5 with 100 mM NaCl) at room temperature as described in "General Coating Procedure". Dry samples were then stained using the Richard-Allan Scientific™ Amyloid Stain kit (Thermo Fisher, Waltham, MA). Samples were placed in alkaline Congo red staining solution for 30 mins in an orbital shaker at 60 rpm at room temperature. Samples were then rinsed with ultrapure water from a squeeze bottle briefly and placed in a dish of ultrapure water on the orbital shaker to wash for an additional 10 mins. Samples were then dried by nitrogen gas and photographed against a white background.

X-Ray Photoelectron Spectroscopy

Chemical composition analysis was performed using a PHI 5600 XPS (PerkinElmer, Waltham, MA) with an ultrahigh vacuum chamber (10^{-9} torr) and a monochromatic Al $K\alpha$ X-ray source operating at 350 W. Dry coatings were prepared on TiO_2 using 2 mg/mL eADF4(C16) with 100 mM KH_2PO_4 and 100 mM NaCl in 25 mM bicine buffer (pH 8.5) for 30 hrs as described above in "General Coating Procedure". Survey scans were taken from a binding energy range of 0 – 1100 eV for 5 mins each. High resolution scans were obtained for C1s (282 – 292 eV), O1s (526 – 536 eV), and N1s (396 – 404 eV) regions for 15 mins each. A neutralizer flood gun was used during scans to counter charging effects.

Spectroscopic Ellipsometry

The thickness of dry coatings on TiO_2 was measured using a M-2000 spectroscopic ellipsometer (J.A. Woollam, Lincoln, NE). Spectra were obtained between 377 – 900 nm at 55°, 60°, and 65° and were fitted to a multilayer model consisting of a silicon substrate, a TiO_2 layer, and a Cauchy layer representing the silk

coating. For each sample, the exact thickness of the clean TiO₂ layer was determined by ellipsometry prior to coating, and this thickness was fixed in the analysis of the sample after coating. The thickness of eADF4(C16) coatings was determined by initiating the Cauchy layer fit with an initial refractive index value of $n = 1.475$. Typical fit results gave $1.47 < n < 1.51$ at 632.8 nm with mean squared error values less than 15.

Contact Angle Measurement

Various substrates were coated by immersion in 0.5 mg/mL eADF4(C16) with 200 mM KH₂PO₄ in 25 mM bicine buffer (pH 8.5, 100 mM NaCl) for 30 hrs at room temperature as described in "General Coating Procedure". The aqueous wettability of coated and uncoated samples was measured using a goniometer with a high-frame-rate video camera and an automated pipet (Ramé-Hart, Succasunna, NJ). For each measurement, 10 μ L ultrapure water was dispensed onto the surface and 100 images were then captured at 10 frames per second. Static contact angle was measured using DropImage analysis software (Ramé-Hart, Succasunna, NJ) and an average of left and right contact angles for 100 images were reported. At least 3 different samples were measured for each condition.

Coating Stability Studies

The stability of eADF4(C16) coatings after prolonged agitation in aqueous solution was characterized using spectroscopic ellipsometry. TiO₂ substrates were coated by immersion in 0.5 mg/mL eADF4(C16) with 200 mM KH₂PO₄ in 25 mM bicine buffer (pH 8.5, 100 mM NaCl) for 20 hrs at room temperature as described in "General Coating Procedure", and the initial thickness of dry eADF4(C16) coatings on TiO₂ was measured. Samples were then agitated in HEPES buffer (pH 7.4, 150 mM NaCl, 37 °C) at 60 rpm in an orbital shaker. After 1, 2, 4, 6, 8, or 11 days of agitation, samples were gently rinsed with ultrapure water, dried with nitrogen gas, and measured by ellipsometry. The eADF4(C16) coating thickness after agitation was normalized to the initial thickness for each sample, and the average normalized thickness for at least 3 samples ($n = 3$) at each agitation timepoint is reported.

Grazing Incidence Wide Angle X-Ray Scattering

To investigate the structure and orientation of β -sheet crystallites in eADF4(C16) coatings, GIWAXS was performed at the SMI beamline (12-ID) of the National Synchrotron Light Source II. Silicon wafers with approximately 2 nm native oxide layer were coated by immersion in 0.5 mg/mL eADF4(C16) with 200 mM KH₂PO₄ in 10 mM bicine buffer (pH 8.5 with 100 mM NaCl) at room temperature for 5 hrs, 10 hrs, and 24 hrs as described in "General Coating Procedure". Samples were measured using a beam energy of 16.1 keV ($\lambda = 0.77 \text{ \AA}$) and an incidence angle of 0.1°. 2D scattering patterns were collected using a rectangular PILATUS3 300K-W detector (Dectris, Baden, Switzerland) with a size of 1475 x 195 pixels and a pixel dimension of 0.172 mm x 0.172 mm. The sample-to-detector distance was 275 mm. The detector was shifted after a 2 s

exposure, giving multiple images that were stitched together using custom software to cover a larger q -space. Stitched detector images were further converted into (q_r, q_z) , where q_r is the in-plane scattering from the sample and q_z is the out-of-plane scattering from the sample. ALBULA Software (Dectris, Baden, Switzerland) was used to perform radial reduction of the (q_r, q_z) scattering images to a 1D intensity vs. $|q|$ plot. Deconvolution analysis was performed in Igor Pro software (Wavemetrics, Portland, OR) using Lorentzian distributions for the scattering contributions arising from the β -sheet crystals while a Gaussian distribution was used for the amorphous halo.

The d -spacings (d_{hkl}) for the Bragg reflections observed were calculated using the peak positions (q_{hkl}) obtained from deconvolution of the 1D reduction using the following equation:

$$d_{hkl} = \frac{2\pi}{q_{hkl}}$$

Furthermore, lattice parameters a , b , and c of the unit cell were solved assuming an orthorhombic crystal structure using the (200), (120), and (121) reflections observed as follows:

$$\frac{1}{d_{hkl}^2} = \frac{h^2}{a^2} + \frac{k^2}{b^2} + \frac{l^2}{c^2}$$

Scanning Electron Microscopy

SEM was performed using a Quanta 3D FEG dual-beam field-emission microscope (FEI, Hillsboro, OR). Dry coatings on TiO₂ were prepared using 2 mg/mL eADF4(C16) with 100 mM KH₂PO₄ and 100 mM NaCl in 25 mM bicine buffer (pH 8.5) for 30 hrs as described above in "General Coating Procedure". Samples were imaged as is (without additional conductive coating) at approximately 10 mm working distance using a secondary electron detector.

Atomic Force Microscopy

AFM height and phase images were obtained using a NanoWizard IIIa AFM (JPK Instruments AG, Berlin, Germany) operated in tapping mode. Imaging in dry state was performed utilizing SSS-NCHR super sharp silicon cantilevers (Nanosensors, Neuchâtel, Switzerland) with a nominal radius of less than 2 nm. Images of hydrated samples in 150 mM NaCl aqueous solution were obtained using ScanAsyst Fluid+ cantilevers (Bruker Nano Inc., Tucson, AZ) with 2 nm radius tip, enabling high-resolution imaging in fluid. Images were collected at 1024 x 1024 pixel or higher resolution and were processed using the JPK data processing software.

AFM nanoindentation of eADF4(C16) coatings in ultrapure water was performed using a JPK ForceRobot 300 (JPK Instruments AG, Berlin, Germany). Soft spherical silicon cantilevers (Nanotools, Munich, Germany) with a spring constant of 0.2 N/m were used with a tip velocity of 1000 nm/s over a z-piezo distance of 500 nm with no dwell time. The contact force was limited to a few nN to minimize indentation depth. The spring constant was determined using the thermal tune method and the tip radius was measured by SEM imaging

to be 23 nm in diameter. To extract the Young's modulus, the force-distance curves were fitted with the Hertz model as shown in Figure S7.^{71,83}

AFM single molecule force spectroscopy measurements were carried out at room temperature using a JPK ForceRobot 300 (JPK Instruments AG, Berlin, Germany) with a tip velocity of 1000 nm/s over a z-piezo distance of 500 nm with 1 s dwell time. The experiments were performed in ultrapure water after allowing the cantilever to equilibrate in solution for at least 30 minutes. MLCT soft silicon nitride cantilevers cantilevers (Bruker Nano Inc., Tucson, AZ) with typical spring constant of 50-60 pN/nm were used for all experiments and calibrated using the equipartition theorem.⁸⁴ The force exerted on the cantilever as the tip retracted from the coating surface was recorded, and at least 50,000 measurements per sample were performed. The percentage of measurements in which protein unfolding events were seen in the force-extension trace, known as the pickup-rate, was <2%. Force-extension traces showing a sawtooth pattern of more than 3 unfolding events were selected for further analysis using data processing software from JPK and custom processing procedures in IgorPro (Wavemetrics, Portland, OR). The spikes in force-extension traces were fitted with a Worm-Like Chain (WLC) model:

$$F = \frac{kT}{p} * \left(\frac{1}{4 \left(1 - \frac{x}{L_c}\right)^2} - \frac{1}{4} + \frac{x}{L_c} \right)$$

where F is the applied force, x is the extension, p is the persistence length, k is the Boltzmann constant, L_c is the contour length, and T is the absolute temperature. Only force-extension traces in which the fit value of $p = 0.4$ nm were considered to be single-molecule measurements. Statistical analysis of the rupture force and L_c values observed in single-molecule measurements was performed using JMP Pro 13 software.

Bacterial Adhesion Assays

Non-pathogenic *S. epidermidis* (ATCC 14990) and *E. coli* (ATCC 25922) obtained from ATCC (Manassas, VA) as frozen stock in glycerol were streaked on tryptic soy agar plates and LB (Miller) plates, respectively. After 18 hrs, a single colony was picked and inoculated into 10 mL broth (tryptic soy for *S. epidermidis* and LB Miller for *E. coli*). Cells were cultured at 37°C in an orbital shaker until mid-log phase, which was determined by absorbance measurement to be 6 hrs for *S. epidermidis* and 2 hrs for *E. coli*. Cells were then centrifuged at 3000 rcf for 5 min, and the pellet was resuspended in sterile-filtered 150 mM NaCl at a concentration of 1×10^8 cfu/mL. Cell concentrations were verified by spreading and culturing million-fold dilutions on Standard Methods Agar plates in triplicate for visual counting of colony forming units.

Stainless steel coupons were coated by immersion in 0.5 mg/mL eADF4(C16) with 200 mM KH_2PO_4 in 25 mM bicine buffer (pH 8.5 with 100 mM NaCl) at room temperature for 3 hrs or 24 hrs as described in "General Coating Procedure". eADF4(C16) was also dissolved in hexafluoroisopropanol (HFIP)

at 1 mg/mL and drop-cast onto clean stainless steel coupons. These drop-cast samples were then placed in a methanol bath for 1 hr, transferred to ultrapure water for 10 mins, and dried with nitrogen gas before use.

For bacterial adhesion assays, samples were placed in 12-well tissue culture plates and were each immersed in 1 mL of 150 mM NaCl containing 1×10^8 cfu bacteria. After 24 hrs for *S. epidermidis* and 48 hrs for *E. coli*, cell solutions were aspirated and coupons were stained using a propidium iodide/SYTO9 viability assay kit (LIVE/DEAD BacLight Bacterial Viability Kit, Thermo Fisher, Waltham, MA). Dye solutions were used at 0.5X concentration and samples were stained for 30 mins in an orbital shaker at 100 rpm. Dye solutions were then gently aspirated and replaced with 150 mM NaCl twice. Finally, coupons were gently rinsed with 5 drops of 150 mM NaCl prior to fluorescence imaging using an EVOS FL microscope (Thermo Fisher, Waltham, MA). Red and green fluorescence images, corresponding respectively to dead and live cells, were taken at 40X magnification from at least 10 random locations (~ 0.57 mm²) on each sample, and 3 samples were examined per condition. The number of live bacteria was counted manually using ImageJ software, and the average live bacteria count per mm² was reported. Statistical analysis was performed in Prism (GraphPad Software, La Jolla, CA) using one-way ANOVA ($\alpha = 0.05$) with Tukey's multiple comparisons post hoc test.

Conflicts of interest

T. S. is co-founder and shareholder of AMSilk GmbH.

Acknowledgements

This research used the SMI beamline (12-ID) of the National Synchrotron Light Source II, a U.S. Department of Energy (DOE) Office of Science User Facility operated for the DOE Office of Science by Brookhaven National Laboratory under Contract No. DE-SC0012704. P. B. M. acknowledges support from NIH grants R37 DE014193 and R01 EB022031. Work by J. B. and T. S. was funded from the DFG grant SFB 840 TPA8. Additional funding for R. H. Z. and J. B. was received from the Bavaria California Technology Center for research-related travel under project 4[2016-2]. The authors additionally wish to thank Anika Winkler (University of Bayreuth) for intellectual discussion.

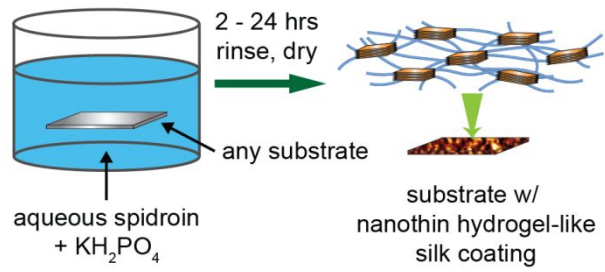
Notes and references

- 1 E. Bull, C. P. Chilton, C. A. L. Gould and T. M. Sutton, *BJU International*, 1991, **68**, 394–399.
- 2 K. A. Kazmierska, R. Thompson, N. Morris, A. Long and T. Ciach, *Urology*, 2010, **76**, 515.e15–515.e20.
- 3 D. M. Siddiq and R. O. Darouiche, *Nat Rev Urol*, 2012, **9**, 305–314.
- 4 C. A. Umscheid, M. D. Mitchell, J. A. Doshi, R. Agarwal, K. Williams and P. J. Brennan, *Infect Control Hosp Epidemiol*, 2011, **32**, 101–114.
- 5 Y. Wang, F. Papatimitrakopoulos and D. J. Burgess, *J Control Release*, 2013, **169**, 341–347.

- 6 B. Yu, C. Wang, Y. M. Ju, L. West, J. Harmon, Y. Moussy and F. Moussy, *Biosens Bioelectron*, 2008, **23**, 1278–1284.
- 7 P. Fattahi, G. Yang, G. Kim and M. R. Abidian, *Adv Mater*, 2014, **26**, 1846–1885.
- 8 Q. Wei and R. Haag, *Mater Horiz*, 2015, **2**, 567–577.
- 9 H. Lee, S. M. Dellatore, W. M. Miller and P. B. Messersmith, *Science*, 2007, **318**, 426–430.
- 10 H. Lee, J. Rho and P. B. Messersmith, *Adv Mater*, 2009, **21**, 431–434.
- 11 K. S. Schanze, H. Lee and P. B. Messersmith, *ACS Appl Mater Interfaces*, 2018, **10**, 7521–7522.
- 12 J. H. Ryu, P. B. Messersmith and H. Lee, *ACS Appl. Mater. Interfaces*, 2018, **10**, 7523–7540.
- 13 H. Lee, Y. Lee, A. R. Statz, J. Rho, T. G. Park and P. B. Messersmith, *Adv Mater*, 2008, **20**, 1619–1623.
- 14 P. Delparastan, K. Malollari, H. Lee and P. Messersmith, *Angew Chem Int Ed*, 2018, in press.
- 15 J. G. Hardy and T. R. Scheibel, *Biochem Soc Trans*, 2009, **37**, 677–681.
- 16 J. G. Hardy, L. M. Römer and T. R. Scheibel, *Polymer*, 2008, **49**, 4309–4327.
- 17 M. Heim, D. Keerl and T. Scheibel, *Angew Chem Int Ed*, 2009, **48**, 3584–3596.
- 18 C. Vepari and D. L. Kaplan, *Prog Polym Sci*, 2007, **32**, 991–1007.
- 19 S. Kapoor and S. C. Kundu, *Acta Biomater*, 2016, **31**, 17–32.
- 20 D. Ebrahimi, O. Tokareva, N. G. Rim, J. Y. Wong, D. L. Kaplan and M. J. Buehler, *ACS Biomater Sci Eng*, 2015, **1**, 864–876.
- 21 A. Leal-Egaña and T. Scheibel, *J Mater Chem* 2012, **22**, 14330–14336.
- 22 A. Leal-Egaña, G. Lang, C. Mauerer, J. Wickinghoff, M. Weber, S. Geimer and T. Scheibel, *Adv Eng Mater*, 2012, **14**, B67–B75.
- 23 S. Sofia, M. B. McCarthy, G. Gronowicz and D. L. Kaplan, *J Biomed Mater Res*, 2001, **54**, 139–148.
- 24 Z. Gao, S. Wang, H. Zhu, C. Su, G. Xu and X. Lian, *Mater Sci & Eng C*, 2008, **28**, 1227–1235.
- 25 L. Meinel, S. Hofmann, V. Karageorgiou, C. Kirker-Head, J. McCool, G. Gronowicz, L. Zichner, R. Langer, G. Vunjak-Novakovic and D. L. Kaplan, *Biomaterials*, 2005, **26**, 147–155.
- 26 I. Dal Pra, G. Freddi, J. Minic, A. Chiarini and U. Armato, *Biomaterials*, 2005, **26**, 1987–1999.
- 27 M. Santin, A. Motta, G. Freddi and M. Cannas, *J Biomed Mater Res*, 1999, **46**, 382–389.
- 28 P. H. Zepelin, N. C. Maksimovikj, M. C. Jordan, J. Nickel, G. Lang, A. H. Leimer, L. Römer and T. Scheibel, *Adv Funct Mater*, 2014, **24**, 2658–2666.
- 29 L. Römer and T. Scheibel, *Prion*, 2008, **2**, 154–161.
- 30 M. Heim, L. Römer and T. Scheibel, *Chem Soc Rev*, 2010, **39**, 156–164.
- 31 D. Huemmerich, C. W. Helsen, S. Quedzuweit, J. Oschmann, R. Rudolph and T. Scheibel, *Biochemistry*, 2004, **43**, 13604–13612.
- 32 S. Ketten and M. J. Buehler, *J R Soc Interface*, 2010, **7**, 1709–1721.
- 33 T. D. Fink and R. H. Zha, *Macromolecular Rapid Communications*, 2018, in press.
- 34 F. Vollrath and D. Porter, *Soft Matter*, 2006, **2**, 377–385.
- 35 Y. Termonia, *Macromolecules*, 1994, **27**, 7378–7381.
- 36 C. Dicko, J. M. Kenney, D. Knight and F. Vollrath, *Biochemistry*, 2004, **43**, 14080–14087.
- 37 D. P. Knight and F. Vollrath, *Naturwissenschaften*, 2001, **88**, 179–182.
- 38 F. Vollrath and D. P. Knight, *Nature*, 2001, **410**, 541–548.
- 39 M. Humenik, A. M. Smith, S. Arndt and T. Scheibel, *J Struct Biol*, 2015, **191**, 130–138.
- 40 T. Scheibel, *Microb Cell Fact*, 2004, **3**, 14.
- 41 M. Humenik, M. Magdeburg and T. Scheibel, *J Struct Biol*, 2014, **186**, 431–437.
- 42 S. Rammensee, U. Slotta, T. Scheibel and A. R. Bausch, *Proc Natl Acad Sci USA*, 2008, **105**, 6590–6595.
- 43 J. D. van Beek, S. Hess, F. Vollrath and B. H. Meier, *Proc Natl Acad Sci USA*, 2002, **99**, 10266–10271.
- 44 J. O. Warwicker, *J Mol Biol*, 1960, **2**, 350–362.
- 45 U. Slotta, S. Hess, K. Spiess, T. Stromer, L. Serpell and T. Scheibel, *Macromol Biosci*, 2007, **7**, 183–188.
- 46 M. Humenik and T. Scheibel, *ACS Nano*, 2014, **8**, 1342–1349.
- 47 A. Lammel, M. Schwab, U. Slotta, G. Winter and T. Scheibel, *ChemSusChem*, 2008, **1**, 413–416.
- 48 N. Helfricht, M. Klug, A. Mark, V. Kuznetsov, C. Blüm, T. Scheibel and G. Papastavrou, *Biomater Sci*, 2013, **1**, 1166–1171.
- 49 U. K. Slotta, S. Rammensee, S. Gorb and T. Scheibel, *Angew Chem Int Ed*, 2008, **47**, 4592–4594.
- 50 S. Rammensee, D. Huemmerich, K. D. Hermanson, T. Scheibel and A. R. Bausch, *Appl Phys A*, 2006, **82**, 261–264.
- 51 X. Wang, H. J. Kim, P. Xu, A. Matsumoto and D. L. Kaplan, *Langmuir*, 2005, **21**, 11335–11341.
- 52 X. Wang, X. Hu, A. Daley, O. Rabotyagova, P. Cebe and D. L. Kaplan, *J Controlled Release*, 2007, **121**, 190–199.
- 53 K. Nakanishi, T. Sakiyama and K. Imamura, *J Biosci Bioeng*, 2001, **91**, 1–12.
- 54 M. Rabe, D. Verdes and S. Seeger, *Adv Colloid Interface Sci*, 2011, **162**, 87–106.
- 55 D. Hall, in *Handbook of Surface Plasmon Resonance*, ed. R. B. M. Schasfoort and A. J. Tudos, Royal Society of Chemistry, London, 2008, ch. 4, pp. 81–122.
- 56 A. Quinn, H. Mantz, K. Jacobs, M. Bellion and L. Santen, *EPL*, 2008, **81**, 56003.
- 57 A. M. Morris, M. A. Watzky, J. N. Agar and R. G. Finke, *Biochemistry*, 2008, **47**, 2413–2427.
- 58 Y. Liu, Z. Shao and F. Vollrath, *Nat Mater*, 2005, **4**, 901–905.
- 59 J. Talbot, G. Tarjus, P. R. Van Tassel and P. Viot, *Colloids Surf A Physicochem Eng Asp*, 2000, **165**, 287–324.
- 60 M. Rabe, D. Verdes and S. Seeger, *Soft Matter*, 2009, **5**, 1039–1047.
- 61 D. S. Hwang and J. H. Waite, *Protein Sci*, 2012, **21**, 1689–1695.
- 62 L. Petrone, A. Kumar, C. N. Sutanto, N. J. Patil, S. Kannan, A. Palaniappan, S. Amini, B. Zappone, C. Verma, and A. Miserez, *Nat. Commun*, 2015, **6**, 8737–12.
- 63 S. Wohlrab, K. Spiess and T. Scheibel, *J Mater Chem*, 2012, **22**, 22050–22054.
- 64 E. Metwalli, U. Slotta, C. Darko, S. V. Roth, T. Scheibel and C. M. Papadakis, *Appl Phys A*, 2007, **89**, 655–661.
- 65 D. T. Grubb and L. W. Jelinski, *Macromolecules*, 1997, **30**, 2860–2867.
- 66 K. Numata, R. Sato, K. Yazawa, T. Hikima, and H. Masunaga, *Polymer*, 2015, **77**, 87–94.
- 67 J. O. Warwicker, *Trans Faraday Soc*, 1956, **52**, 554–555.
- 68 R. E. Marsh, R. B. Corey, and L. Pauling, *Acta Cryst*, 1955, **8**, 62.
- 69 U. Slotta, M. Tammer, F. Kremer, P. Koelsch and T. Scheibel, *Supramolecular Chemistry*, 2006, **18**, 465–471.
- 70 F. Vollrath and D. Porter, *Appl Phys A*, 2006, **82**, 205–212.
- 71 D. C. Lin, E. K. Dimitriadis and F. Horkay, *J Biomech Eng*, 2007, **129**, 430–440.
- 72 K. N. Savage and J. M. Gosline, *J Exp Biol*, 2008, **211**, 1948–1957.
- 73 K. Spieß, R. Ene, C. D. Keenan, J. Senker, F. Kremer, and T. Scheibel, *J Mater Chem*, 2011, **21**, 13594–13604.
- 74 M. P. Neubauer, C. Blüm, E. Agostini, J. Engert, T. Scheibel and A. Fery, *Biomater Sci*, 2013, **1**, 1160–1165.
- 75 R. Liu, Q. Deng, Z. Yang, D. Yang, M.-Y. Han and X. Y. Liu, *Adv Funct Mater*, 2016, **26**, 5534–5541.
- 76 E. Oroudjev, J. Soares, S. Arcidiacono, J. B. Thompson, S. A. Fossey and H. G. Hansma, *Proc Natl Acad Sci USA*, 2002, **99**, 6460–6465.

- 77 Z. Huang, P. Delparastan, P. Burch, J. Cheng, Y. Cao and P. B. Messersmith, *Biomater. Sci.*, 2018, **6**, 2487-2495.
- 78 W. Ott, M. A. Jobst, M. S. Bauer, E. Durner, L. F. Milles, M. A. Nash and H. E. Gaub, *ACS Nano*, 2017, **11**, 6346-6354.
- 79 G. Stirnemann, D. Giganti, J. M. Fernandez and B. J. Berne, *Proc Natl Acad Sci USA*, 2013, **110**, 3847-3852.
- 80 S. Wohlrab, S. Müller, A. Schmidt, S. Neubauer, H. Kessler, A. Leal-Egaña and T. Scheibel, *Biomaterials*, 2012, **33**, 6650-6659.
- 81 F. Bauer, S. Wohlrab and T. Scheibel, *Biomater. Sci.*, 2013, **1**, 1244-1249.
- 82 G. Lang, S. Kumari, E. DeSimone, C. Spengler, S. Lücker, M. Hudel, K. Jacobs, N. Krämer and T. Scheibel. *manuscript in submission*.
- 83 E. Dimitriadis, F. Horkay, J. Maresca, B. Kachar and R. Chadwick, *Biophys J*, 2002, **82**, 2798-2810.
- 84 J. Lübbe, M. Temmen, P. Rahe, A. Kühnle and M. Reichling, *Beilstein J Nanotechnol*, 2013, **4**, 227-233.

Table of Contents Entry



Biomimetic spidroin self-assembly allows formation of substrate-independent one-pot nanofiber silk coatings.